Colloids and Surfaces A 553 (2018) 660–671

Contents lists available at ScienceDirect

Colloids and Surfaces A

journal homepage: www.elsevier.com/locate/colsurfa

Image analysis of axisymmetric droplets in wetting experiments: A new tool for the study of 3D droplet geometry and droplet shape reconstruction

Inmaculada Ríos-López[a], Polykarpos Karamaoynas[b], Xenophon Zabulis[b], Margaritis Kostoglou[a], Thodoris D. Karapantsios[a,*]

[a] Division of Chemical Technology, School of Chemistry, Aristotle University, University Box 116, 541 24, Thessaloniki, Greece
[b] Institute of Computer Science, Foundation for Research and Technology, Hellas, N. Plastira 100 Vassilika Vouton, 700 13, Heraklion, Crete, Greece

GRAPHICAL ABSTRACT

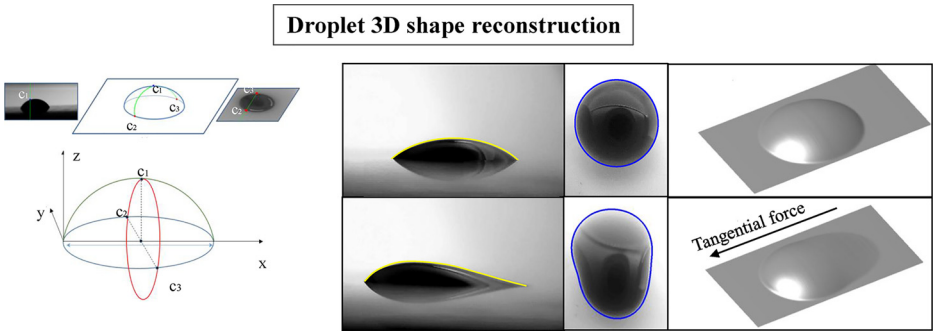

ARTICLE INFO

Keywords:
Image processing
Forced wetting
3D droplet shape reconstruction
Non-axisymmetric droplets
Droplet spreading/sliding

ABSTRACT

A new software tool is developed for droplet image analysis for the study of wetting of solid substrates. The tool extracts information exclusively from images and does not require the use of any properties of the system. Moreover, its applicability covers both axisymmetric and non-axisymmetric droplets. The developed software processes independently droplet images taken from side and top perspectives. Processing of side-view images is made by polynomial fitting to the droplet shape and provides important 2D geometrical features such as contact angles, length, height, contact point coordinates and contour outline. The analysis of top-view images is achieved through active contours (snakes) and yields droplet dimensions, centroid position and contour outline. The combination of synchronized side and top images provides the reconstruction of the droplet 3D shape by means of slices of circular arc shape, which allows estimation of droplet volume and of the distribution of contact angles along its perimeter. The above is an important feature that has not been delivered by other software tools. Experimental results to support the applicability of the new tool are presented for two distinct substrates having different surface properties (glass and Teflon).

1. Introduction

The continuously increasing number of publications related to wetting reveals the importance of this only partially understood phenomenon [1]. When studying wetting, the most relevant information is extracted from images in which the spreading or sliding of droplets over substrates is captured. Several tools and methods have been introduced along the years for the analysis of such images for

* Corresponding author.
E-mail address: karapant@chem.auth.gr (T.D. Karapantsios).

https://doi.org/10.1016/j.colsurfa.2018.05.098
Received 21 March 2018; Received in revised form 30 May 2018; Accepted 31 May 2018
Available online 06 June 2018
0927-7757/

extracting droplet geometrical features that are essential to determine the wetting behavior of a solid-liquid system [2]. In this context, the feature most commonly measured to study wetting of liquid/solid combinations is the contact angle, which is defined as the angle between the tangent plane to the liquid-vapor interface and the tangent plane to the solid-liquid interface, at the point where the three phases (solid, vapor and liquid) meet [3]. This parameter was first introduced by Thomas Young in 1805 [4] and its relation to the different interfacial tensions between interfaces is expressed in Eq. (1).

$$\sigma_{sv} = \sigma_{sl} + \sigma_{lv}\cos\theta \quad (1)$$

where σ_{sv} is the interfacial tension between solid and vapor, σ_{sl} is the interfacial tension between solid and liquid, σ_{lv} is the interfacial tension between liquid and vapor and θ is the equilibrium contact angle. The contact angle value determines the degree of wettability of a solid by a specific liquid. Surfaces are classified as wettable when their contact angle ranges from 0 to 90°, and as non-wettable when it ranges from 90 to 180° [5]. Regardless of the conceptual simplicity of contact angle, the actual measurement of accurate contact angles depends on the specific solid/liquid homogeneity and the employed methodology [6]. In practice, when a droplet is deposited on top of a surface, a range of contact angles can be obtained. This range is known as Contact Angle Hysteresis (CAH) and its maximum and minimum limits are known as advancing (θ_A) and receding (θ_R) contact angle, respectively [7]. These angles can be measured applying external forces to the system such as gravitational, centrifugal, electrical, etc. In the specific case in which centrifugal forces are applied, when rotation speeds are low, a spreading stage may occur in which the droplet deforms and moves partially due to local instabilities at the front part. The front edge moves in the direction of the tangential force with the advancing contact angle, θ_A. During the spreading stage, the rear part of the droplet is pinned to the substrate with which it attains an angle whose value ranges between the initial and the receding contact angle [8]. If the rotation speed increases, the angle attained in the rear part of the droplet reaches the value of the receding contact angle, θ_R. At this moment, the droplet detaches from the surface and slides in the direction of the force. The detachment of the droplet from the surface occurs when a critical tangential force is applied. For a specific solid-liquid pair, this critical force depends also on droplet volume. Nevertheless, when deposited over different substrates, the spreading/sliding behavior of a droplet of the same liquid and the same volume can differ extremely in terms of the tangential force needed for the evolution of droplet shape and eventually its motion.

Regarding the measurement of contact angles, two groups of procedures have been used: tensiometric and goniometric methods. On the one hand, tensiometric methods employ Eq. (1) to calculate the equilibrium contact angle (θ) of symmetric droplets, while measuring interfacial tensions (σ) independently. Nevertheless, as mentioned above, the equilibrium contact angle is not a realistic quantity due to substrate heterogeneities, roughness or adsorption of vapor onto the solid surface [9]. On the other hand, goniometric methods are image-analysis based and extract the droplet shape directly from the acquired images. Within goniometric methods, two families of different procedures can be found. On the first, methods such as Axisymmetric Droplet Shape Analysis (ADSA) are included. ADSA is a goniometric method widely used which determines with high accuracy the droplet shape comparing it with the ideal shape obtained by Young-Laplace equation [3,10]. Nevertheless, this method allows only to evaluate symmetric droplets and, furthermore, extensive knowledge of the system properties is required to estimate the theoretical droplet shape [11]. In contrast, the second family of goniometric methods is based in pure image-analysis. A common first step for these latter methods is the fitting of a theoretical curve to the droplet contour [12]. For small droplets placed on a horizontal surface, the shape of the liquid-vapor interface can be approximated by a circle when viewed from the side [13]. However, for large droplets gravity leads the liquid to flatten, which is a reason that the droplet shape is best approximated by an ellipse [14]. At this point it is important to highlight that these assumptions (both for small and large droplets) are met only for symmetric droplets. However, in most applications, droplets are exposed to a combination of external forces that cause the contact line to be distorted from symmetry, and methods to analyze non-axisymmetric droplets are therefore essential. Among the methods developed to this purpose, important contributions are the Sub-Pixel Polynomial Fitting (SPPF [15],) or the recently developed method by Mirzaei [16], who uses a moving goniometric mask instead of fitting a polynomial function to find the contact angles.

Overall, as shown above, measuring both advancing and receding contact angles is essential to characterize wetting of a liquid on a solid surface. However, full understanding of the phenomenon requires additionally precise knowledge of the droplet's shape [3]. For instance, while side-view images are suitable to determine contact angle and other geometrical features of the droplet such as its length, height or sliding velocity, they are not sufficient to define its shape because the shape is defined by two interfaces: i) the solid-liquid interface and ii) the liquid-vapor interface. First, the solid-liquid interface is a two-dimensional (2D) closed-shape confined by the three-phase contact line where solid, liquid and vapor phases intersect [17]. Characterizing this interface is important in multiple applications, such as to compute the wetted area [18], to measure geometrical factors for the calculation of the retention force [19,20], or to explore the different pinning/depinning behavior of the front and rear regions of a droplet sliding over an inclined surface [8]. When the droplet is placed on horizontal surfaces, this interface is always circular. However, its shape is deformed when external forces are applied. For instance, on tilted substrates, gravity acts inducing the deformation of the solid-liquid interface [21]. For this reason, when droplets are subjected to external forces, images taken from above, in a parallel direction to the substrate, (top-view) are needed to explore the shape of the three-phase contact line. Once observed from the top-view, the next step is to parametrize the shape of the interface, which depends at the same time on the specific solid-liquid pair used and on the applied forces. Therefore, as a function of these latter aspects, several approximations for the geometry of the three phase contact line have been proposed (e.g. parallel-sided [22], asymmetrically elongated [23], or elliptical [24]). The second interface delimiting the droplet shape is the vapor-liquid interface. This is a three-dimensional (3D) surface and is determined by the interplay between surface tension and gravity (or other external forces). For small droplets on horizontal substrates, this 3D surface can be approximated by a spherical cap [25]. In this case, the effect of gravity is small and the shape follows the Laplace minimum energy principle [26]. However, when the droplet volume is large, its shape is flattened due to gravity [27]. For a droplet sliding due to the imposition of external forces, the shape is not symmetric and cannot be approximated by a spherical cap or a flattened sphere. The droplet is deformed in the direction of the force and attains the advancing and receding contact angles in the front and rear edges, respectively. To be able to determine the 3D shape of the liquid-vapor interface it is necessary to define all the angles along the perimeter, whose value lies between the advancing and receding contact angles. To describe the distribution of contact angles along the droplet perimeter, several approximations have been proposed fitting different polynomial functions to the contact angle variation ([3,28]). ElSherbini et al. [24] developed a new device for the exploration of droplet shape on a tilted plate using a rotating camera to take side-images for every azimuthal coordinate along the droplet perimeter. The azimuthal coordinate φ is defined on the droplet three-phase contact line and its value is 0° for the front point and 180° for the rear. The profile images were used to characterize the nature of the contact angle function $\theta(\varphi)$ with $\theta(\varphi = 0) = \theta_{front}$ and $\theta(\varphi = 180) = \theta_{rear}$, and the experimental findings were best fitted by a 3rd degree polynomial. An alternative method to obtain the distribution of angles along the perimeter would be to use a side and a top camera and combine the images obtained from both perspectives to reconstruct the 3D shape of the

liquid-vapor interface.

The main goal of this paper is to present a new software for the study of wetting under external body forces that is able to extensively characterize the droplet shape in terms of both the solid-liquid and the liquid-vapor interfaces. To this aim, this new tool performs the droplet characterization in two steps: first, top and side images are analyzed to extract 2D geometrical features such as contact angles, length, height, width, contact point position and contour outlines. Thereafter, top and side contours are combined to obtain a 3D reconstruction of the droplet. To the best of our knowledge, the latter constitutes a unique feature offered by the present software. Finally, several experiments, carried out in *Kerberos* ([29,30]), are presented to assess the performance of the newly developed software under different wettability conditions comparing a hydrophilic (glass) and a slightly hydrophobic (Teflon) substrate.

2. Methodology

Droplet images acquired from top and side views are analyzed independently to extract contour outlines. These contours are employed to compute 2D geometrical droplet features whereas their combination avails the 3D reconstruction of the droplet shape. The Matlab® software (v. 2013) has been used for the implementation of the application.

In principle, the movement of a droplet over a planar substrate is considered and recorded by two cameras (side and top view) providing orthogonal perspectives of the phenomena as shown in Fig. 1.

Regarding the positions of the cameras, the side camera is placed in such a way that its imaging plane is perpendicular to the substrate. The side camera images the substrate profile as a straight line, which will henceforth be denoted as “horizon” as seen in Fig. 1. The top camera is placed with its imaging plane parallel to the substrate and monitors the droplet movement from above. Furthermore, a third camera is employed to record the droplet from the back. The images acquired by the back view camera are used only to assure initially the symmetry of the droplet and, in particular, the symmetry during the onset of its movement over the solid surface. The three cameras are synchronized to allow registering the complete evolution of the droplet shape with time.

Once the cameras and magnifying lenses are fixed in place, calibration is carried out independently for side and top cameras. The calibration process aims at determining the conversion factor from pixel distances to metric length units (mm). The aforementioned procedure is achieved by measuring the image size of reference objects and allows calibration for each particular droplet-camera/lens distance. It is assumed that this distance remains constant throughout the recording. Lens distortion and perspective foreshortening at the periphery of the images are considered negligible.

The camera recordings are saved as video files (in AVI format) from which the software extracts image frames for subsequent analysis. Afterwards, a Region of Interest (ROI) is selected in images and only the image regions enclosed within these limits are further processed. From this stage on, the approaches used for the side and top view images processing are different and are explained separately.

2.1. Side view processing

The processing of the side view images starts with the manual selection of the horizon in the image (yellow horizontal line in Fig. 2(a)). The horizon has been previously defined in Fig. 1 as a straight line seen from the side camera and represents, physically, the three phase contact line where liquid, vapor and solid meet. The droplet is located above the horizon and is recognized against the background using edge detection [31] and foreground segmentation by intensity thresholding based on the assumption that the droplet is darker than the background. The threshold for the segmentation is adaptive [32], but its value can be also determined by the user. This flexibility provides the means to analyze images with different illumination that may have different grey levels for both droplet and background (Fig. 2(b)). The contour of the droplet is outlined and finely interpolated. Initial contour points are moved towards the closest image edge (as detected by [31]) in the direction of the image gradient at their initial location to achieve a more accurate outline.

Edge diffraction is a common source of error on the accurate detection of image borders. It is apparent that for the mobile gas/liquid interface of a droplet where light reflections vary with the droplet shape it is not easy to quantify the effect. This might be the reason that many published articles [11,15] do not even mention the problem and proceed with droplet edge detection based on the highest contrast gradient or other pure optical techniques. On this account, the aforementioned analysis has been validated by comparing contact angle values determined by the present software with contact angles determined manually assuming that the droplet edge is at the boundary of the dark region in captured images. The maximum difference between measurements is about ± 2°. Differences are arbitrary with no clear trend among images. Such small deviations do not invalidate the present results. This is more so if one takes into account the repeatability in the current estimations which is ± 1° (see below). Work is underway to incorporate adjustments to the software to cope with edge diffraction on moving liquid interfaces.

The droplet contour shape nearby the edges determines the right (θ_{Right}) and left (θ_{Left}) contact angles (Fig. 2(c)). For the contact angle estimation, a polynomial fitting is applied to increase the robustness of the procedure to potential contour tracing errors and pixel

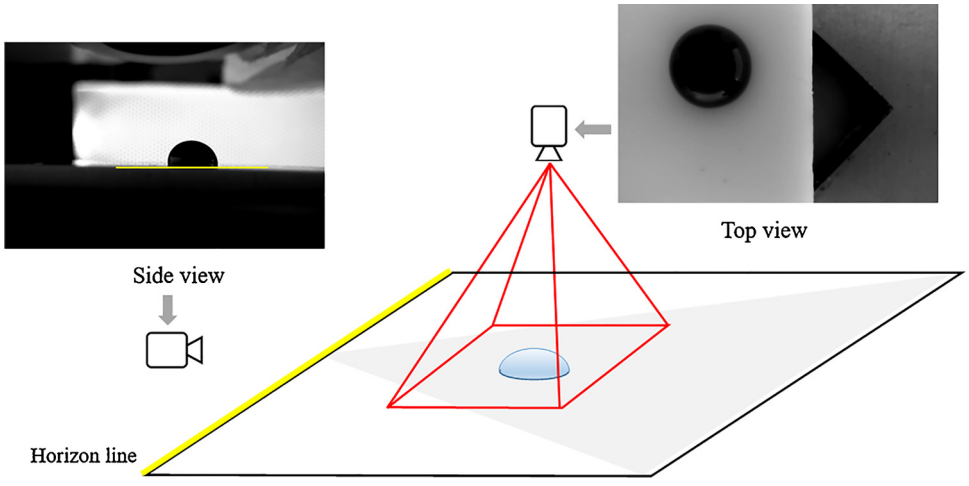

Fig. 1. Illustration of side and top camera positions and examples of the acquired images.

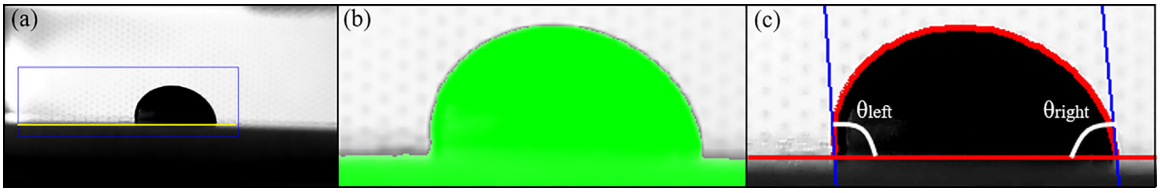

Fig. 2. Side view processing overview. (a) ROI (blue) and horizon (yellow) definition (b) image segmentation (c) contour extraction (red), computation of the tangent (blue) and estimation of contact angles in left (θ_{Left}) and right (θ_{Right}) edges of the droplet. (For interpretation of the references to colour in this figure legend, the reader is referred to the web version of this article.).

quantization. Afterwards, the tangent to the polynomial at the contact point is identified, and the angle between this tangent and the horizon is computed.

In the first place, contour points in the neighborhood of the two edges are selected to perform the polynomial fitting independently and bilaterally. Several contour points *k* are extracted starting from the edge towards the center of the droplet. The number of *k* points can be regulated by the user as a percentage of the total contour points. The default value of *k* is set at 0.3, meaning that the 30% of the contour points closest to the edge will be extracted and used for the polynomial fitting. Thereafter, a polynomial is fitted to the points and the fitting determines the weighting factors a_i, in Eq. (2):

$$f(x) = a_n x^n + a_{n-1}x^{n-1} + \ldots + a_2 x^2 + a_1 x + a_0 \quad (2)$$

The polynomial grade *n* in Eq. (2) can be selected by the user, but its optimal value is also investigated experimentally. For this purpose, values for *n* from 1 to 9 are tested to find the one that best fits the contour at the droplet edges. Grade 1 (line) is discarded as the shape of the droplet contour is a curve. By empirical evaluation of a wide range of examples (droplets), the polynomial grade that for most datasets yields the closest result to the actual contour (ground truth) is the value 4. As seen in Fig. 3, polynomial grades equal to 7 and greater yields over-fitted curves with concavities upward nearby the edges. Consequently, in these cases, the computed tangent line lies inside the droplet providing unacceptable results for contact angles.

Once the polynomial is fitted, the contact points $\boldsymbol{p} = [p_x, p_y]^T$ are located in the intersection of the polynomial curve with the horizon line in both edges of the droplet. The identification of the contact points is a crucial step of the processing since contact angles are computed on these points. In order to estimate the contact angle, the tangent line to the polynomial curve is computed at the point p_x as the derivative of the polynomial function as expressed in Eq. (3).

$$f(x) = a_n x^n + a_{n-1}x^{n-1} + \ldots + a_2 x^2 + a_1 x + a_0 \quad (3)$$

Since the line is tangent to the polynomial, the inclination, *m*, of the tangent line should be equal to the value of the derivative of *f* at p_x, or otherwise $f'(p_x) = m$. The derivate of *f* is analytically predicted using Eq. (4).

$$f'(p_x) = n a_n p_x^{n-1} + (n-1)\, a_{n-1} p_x^{n-2} + \ldots + 2a_2 p_x + a_1 \quad (4)$$

which is used to find the value of *m*. Using *m* and solving for *y* in the general equation of the tangent (The Slope-Intercept Form of the

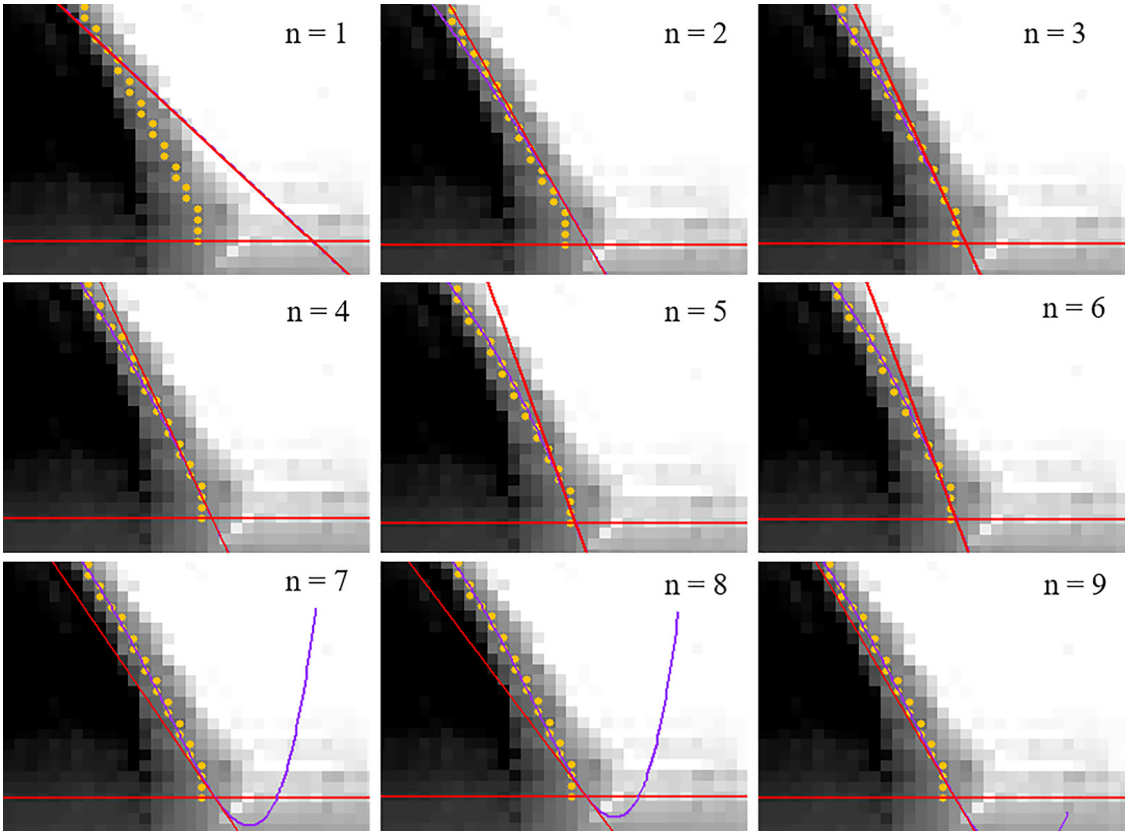

Fig. 3. Experimental results for contour points (orange), polynomial fitting (purple) and tangent line (red) for several polynomial grades, n (1–9). (For interpretation of the references to colour in this figure legend, the reader is referred to the web version of this article.).

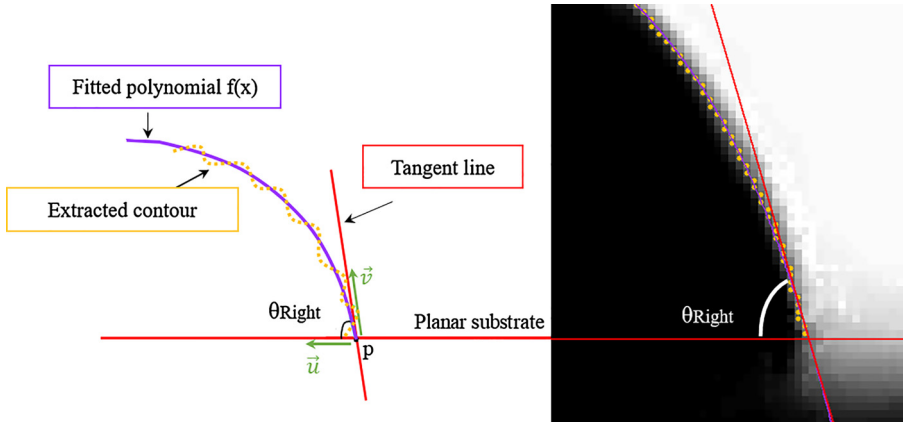

Fig. 4. Estimation of the contact angle in the right contact point (θ_{Right}) from the horizon vector ($\vec{u}$) and the tangent vector ($\vec{v}$).

equation of a straight line: y = mx + b), $m = \frac{y-p_y}{x-p_x}$ avails the equation of the tangent line at **p** as calculated in Eq. (5).

$$f_2(x) = m \cdot x - m \cdot p_x + p_y \tag{5}$$

Bearing in mind that the contact angle is the angle between the tangent line and the horizon at the location of the contact point ***p***, the left and right contact angles (θ_{Right} and θ_{Left}, respectively) are computed as follows. Defining $\vec{u}$ as the vector from point ***p*** on the horizon line and $\vec{v}$ as the vector from point ***p*** on the tangent line, the estimated contact angle is given by $\cos^{-1}\theta_{Right} = \frac{u \cdot v}{|u| * |v|}$, as represented in Fig. 4.

Generally, the contact angle formed by liquids deposited onto solid surfaces ranges from 0 to 180° and therefore, the processing should admit any value within these limits. Two different cases can be identified: hydrophilic surfaces provide contact angle values between 0 and 90°, whereas hydrophobic surfaces provide values ranging from 90° to 180°. The aforementioned cases are processed in a different way and hence the software must be able to classify them. Algorithmically, the software can distinguish these two cases comparing the ratio of dimensions of the bounding box of the contour (Fig. 5). Hydrophobic substrates (Fig. 5(a)) yield a bounding box with a larger vertical dimension. In contrast, hydrophilic substrates (Fig. 5(b)) yield a larger horizontal dimension of the bounding box.

In the hydrophobic case, various points of the contour have the same x values (Fig. 5(a)), thus the parameterization of the contour cannot be achieved with a function, which needs a one to one, $x \rightarrow y$ relation. Alternatively stated, for a given x the function should return a unique $y = f(x)$ value. This premise is violated in the hydrophobic case, i.e. points p_1 and p_2 in Fig. 5(a). In this case, the processing starts with the rotation of the contour 90° clockwise about the image center. The estimation of the tangent is therefore carried out in the rotated image and the results are converted to the initial reference system performing the inverse rotation (90° anticlockwise).

In the hydrophilic case, all contour points have different x values and, thus, function f is directly fitted to the contour points. The least-squares method [33,34] on Y distance from the curve is used for this fitting, in both cases, where Y is the vertical (y-axis) distance between the segments points and the fitted curve. In all cases, the average error in the measurements is estimated to be ± 1°.

2.2. Top view processing

Based on the assumption that the droplet is darker than the background, an active contour approach (snakes) is employed to find the droplet contour in the top view. The procedure followed for the processing of the top view images is illustrated in Fig. 6.

First, initialization of the active contour provides a rough estimation of the foreground segmentation (Fig. 6(b)). This initialization is performed by a rough intensity thresholding segmentation, using the approach in Section 2.1. Threshold value is now not automatically determined, but is set conservatively, so as the contour reliably includes the droplet in the image. Thereafter, the active contour converges to better approximate the droplet outline (Fig. 6(c)). In the present formulation, both contrast and image edges are used to attract contour convergence [35]. It must be noted that the abovementioned method can only be applied to closed shapes. This is why it is not appropriate to process side view images [36].

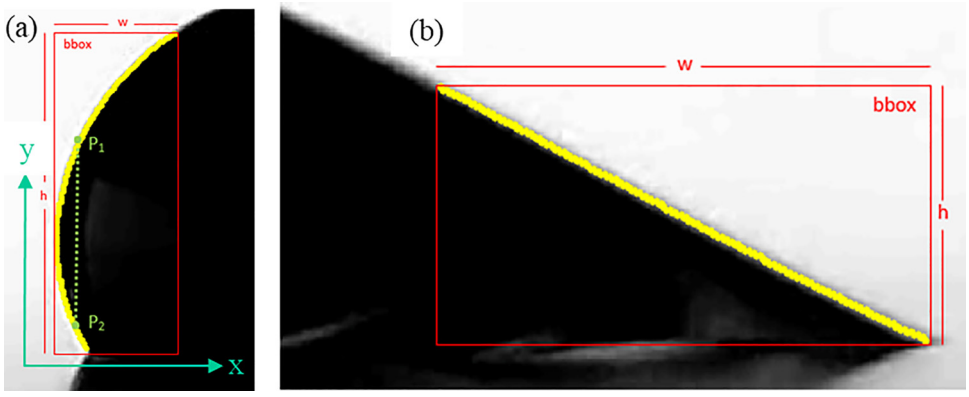

Fig. 5. Bounding box (bbox) proportions for a droplet placed on top of (a) hydrophobic and (b) hydrophilic substrates stressing the dimensions of w (width) and h (height) of the box.

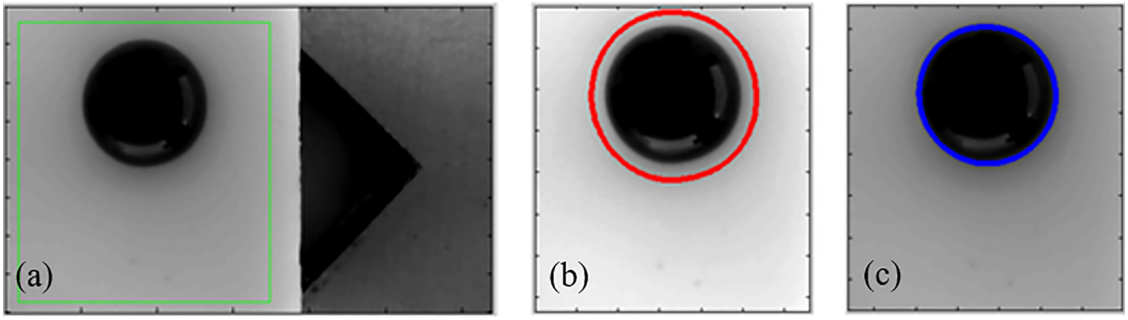

Fig. 6. Top view processing overview. (a) ROI definition, (b) rough contour extraction, (c) fine contour tracing based active contours.

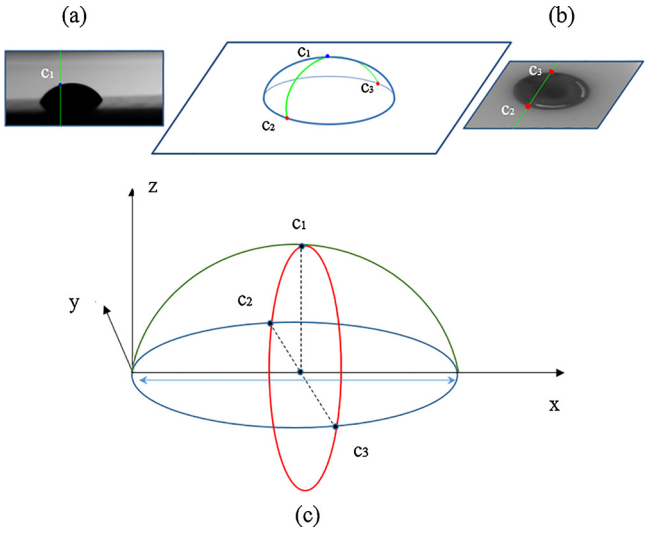

Fig. 7. 3D reconstruction principles (a) Location of c_1 in the droplet side view, (b) location of c_2 and c_3 in the droplet top view, (c) circular intersection of the slice and the droplet surface.

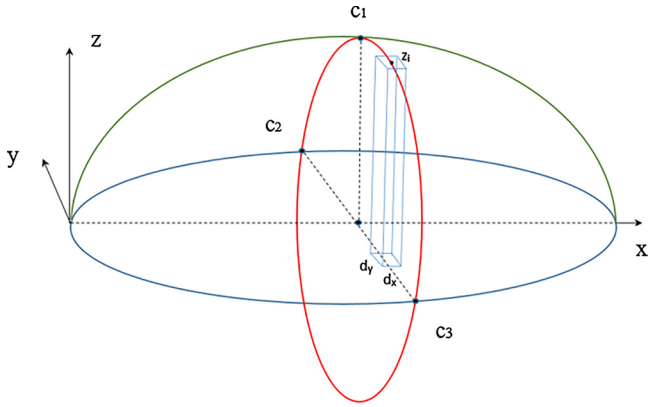

Fig. 9. Measured volume from the 3D shape by adding up the volumes of prism (dx, dy, dz).

2.3. 3D reconstruction

In addition to 2D geometrical droplet features extracted from individual side and top view images, the combination of both side and top view contours allows reconstructing of the 3D droplet shape. The droplet volume is built in "slices" which are defined as hypothetical planes parallel to the *yz* plane and, accordingly, perpendicular to the substrate. The intersection of each of these planes with the droplet surface is approximated by a circle as illustrated with a red circle in Fig. 7(d). In addition, the circle contains three points that are known from previous processing. These points are: the highest point from the side view for the corresponding x coordinate and for which $y = 0$ (c_1, blue dot in Fig. 7(a)) and the 2 points from the top image that belong to the substrate plane ($z = 0$) for the same x coordinate (c_2 and c_3, red dots in Fig. 7(c)). In this way, the circle is defined as illustrated in Fig. 7(d) for every x coordinate along the whole droplet length and compiled to reconstruct the droplet 3D volume as a point cloud. The approximation of the droplet shape by circular arcs has been inspired by its successful use as a tool to solve the three dimensional Young-Laplace equation [37]. Such approximation has some limitations but it fits nicely the present results. Given the calibration information, contour points are converted from pixel to 3D coordinates. Finally, by concatenating points from neighboring slices, the 3D surface that approximates the droplet shape is computed.

Fig. 8 exemplifies the achievement of the 3D shape (Fig. 8(c)) through the combination of the side (Fig. 8(a)) and top (Fig. 8(b)) contours for axisymmetric (upper row) and non-axisymmetric (lower

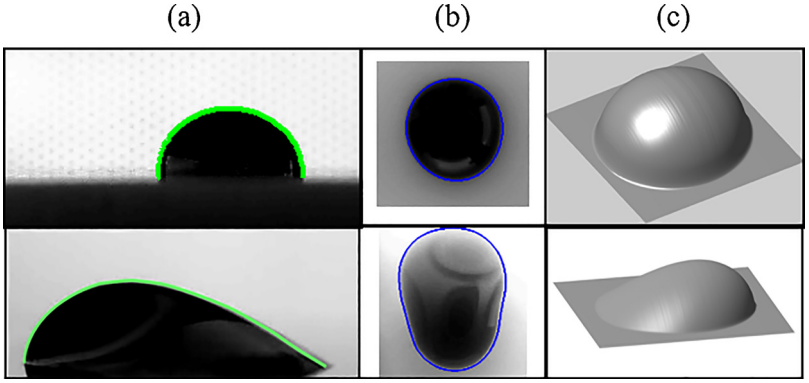

Fig. 8. 3D reconstruction examples pointing out droplet contour from (a) side and (b) top views and (c) the resulting 3D shape for axisymmetric (upper row) and non-axisymmetric (lower row) droplets.

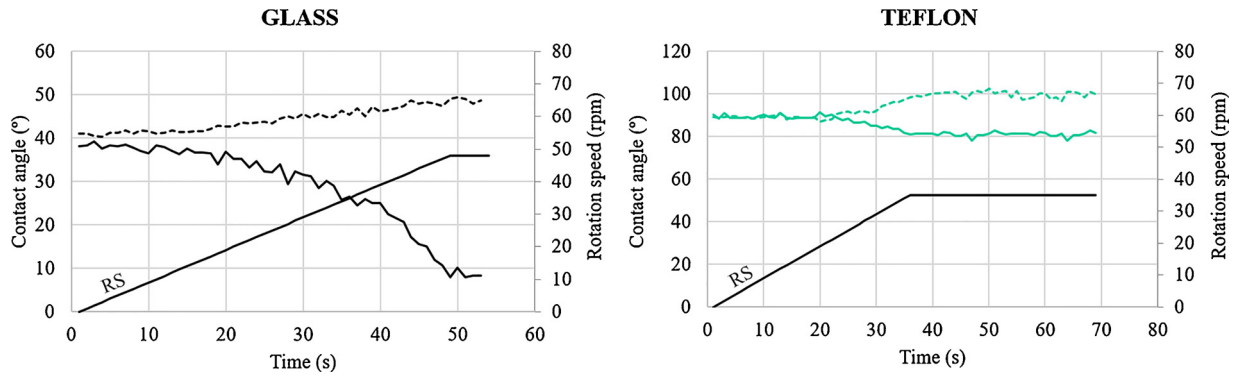

Fig. 10. Front (θ_f, dashed line) and rear (θ_r, solid line) contact angles evolution versus time for a 20 µL droplet over (a) Glass, (b) Teflon. Rotation speed (*RS*) increases with a rate of 1 rpm/s until the target speed is reached (a) 48 rpm, (b) 35 rpm.

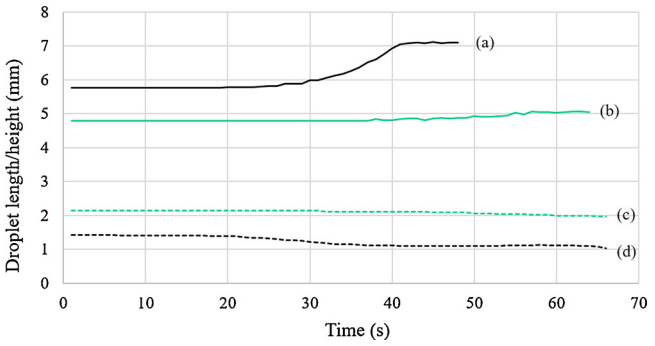

Fig. 11. Droplet length/height evolution versus time for a 20 µL droplet sliding over glass and Teflon. (a) Length on glass, (b) Length on Teflon, (c) Height on Teflon, (d) Height on glass. Rotational speed increases by 1 rpm/s.

row) droplets.

In the 3D reconstruction, the droplet volume is computed as shown in Fig. 9. The volume is defined as $V = d_x \cdot d_y \cdot \sum_{i=1}^{n \cdot m} z_i$ where *dx, dy* are system configuration parameters (i.e. can be defined by the user).

Having reconstructed the 3D droplet shape the contact angle distribution along the three phase contact line is computed by numerical differentiation.

2.3.1. Geometrical measurements

The processing of the side view images provides 2D geometrical measurements such as contact angles, contact points and highest point positions. Using such information, other geometrical properties can be computed, for example, length and height. In the top view, apart from the droplet perimeter and contact area, the droplet centroid ***C*** is computed as the center of the axis-aligned of the bounding rectangle of the top view contour.

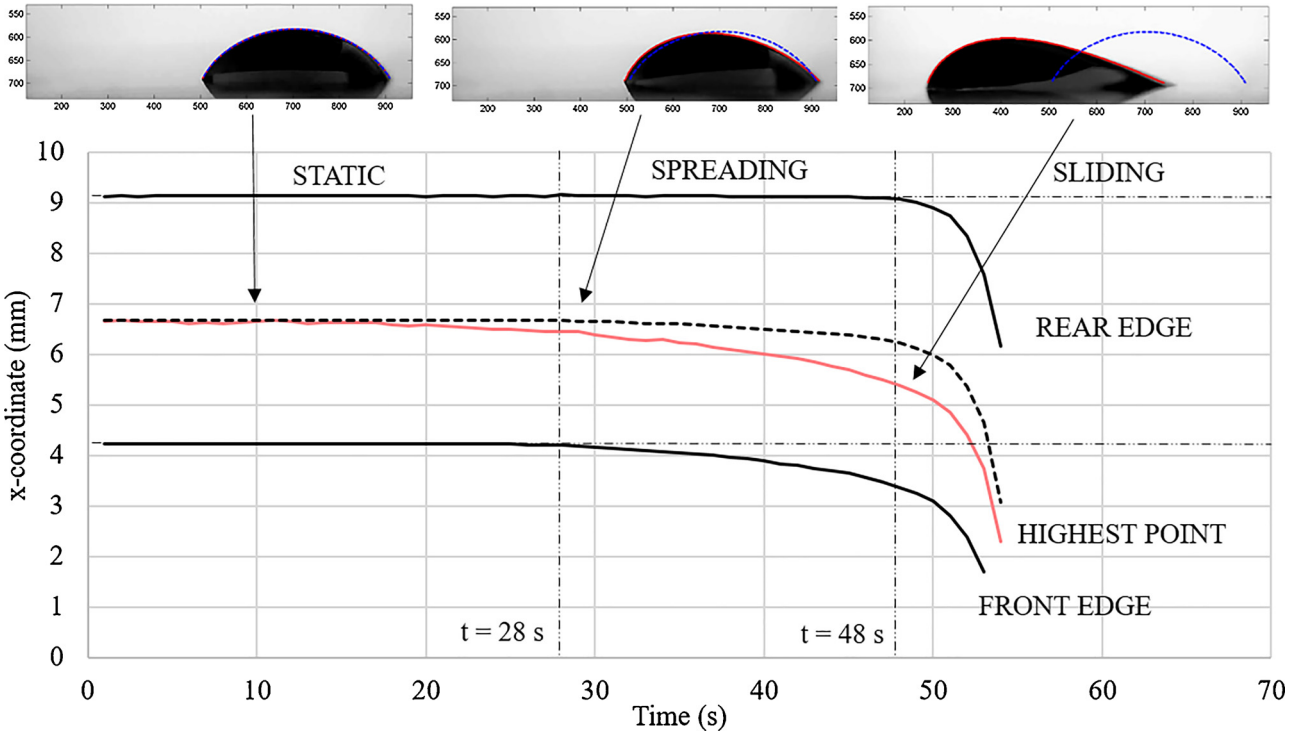

Fig. 12. Sliding of a 20 µL droplet over glass. Position of front and rear edges and the highest point in the x-axis (solid). Also, middle distance between edges position (dashed). Rotational speed increases by 1 rpm/s.

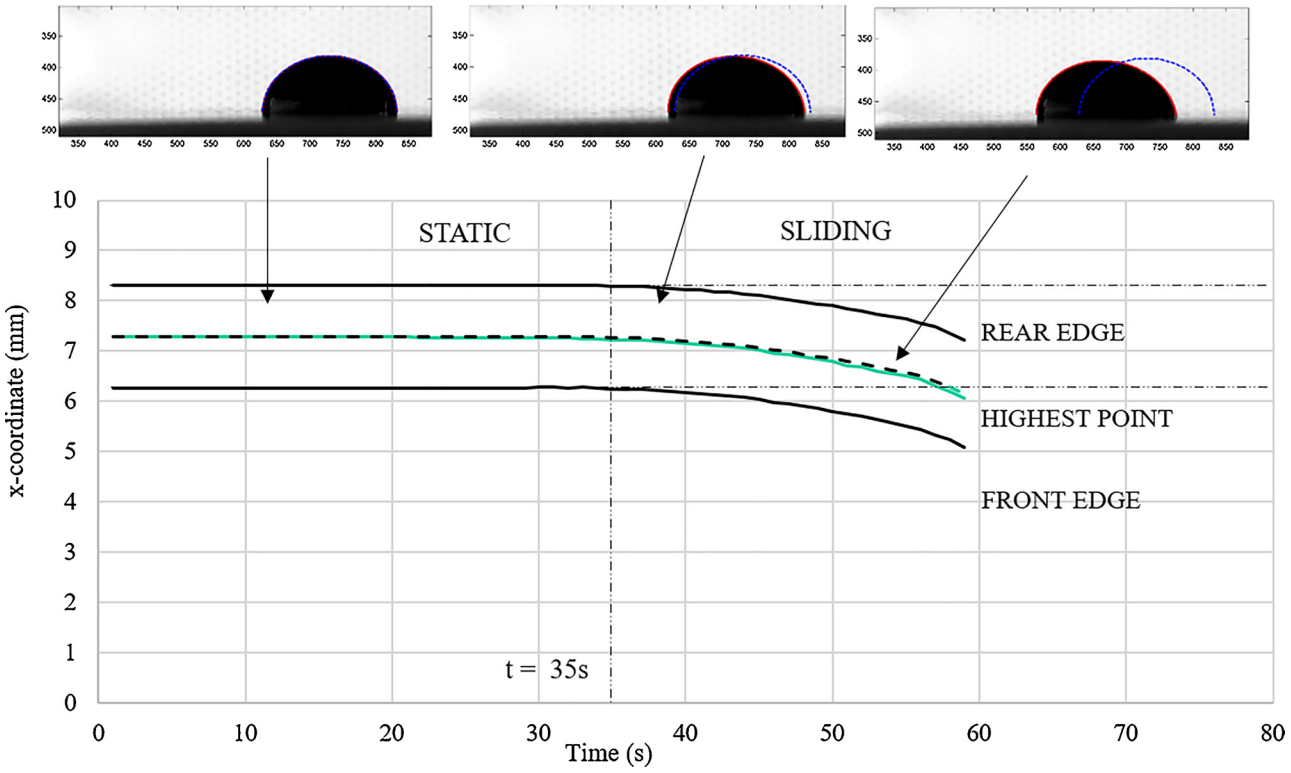

Fig. 13. Sliding of a 20 µL droplet over Teflon. Position of front and rear edges and the highest point in the x-axis (solid). Also, middle distance between edges position (dashed). Rotational speed increases by 1 rpm/s.

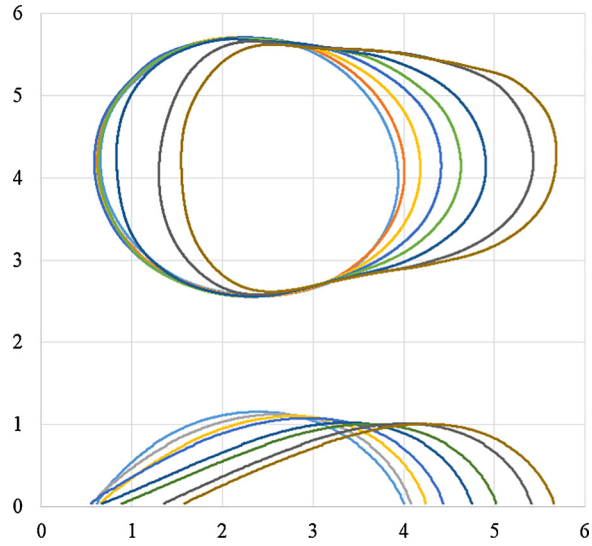

Fig. 14. Top (up) and side (bottom) droplet contour evolution of a 20 µL droplet sliding over glass.

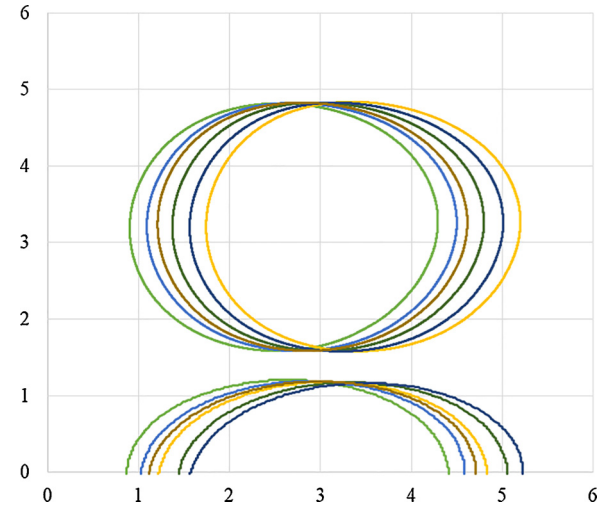

Fig. 15. Top (up) and side (bottom) droplet contour evolution of a 20 µL droplet sliding over Teflon.

In addition to static geometrical properties extracted from individual frames, dynamic measurements are also available. The angle and length variation rates are computed performing derivatives of individual measurements using Gaussian smoothing to reduce inaccuracies and noise. Using temporal derivatives, the spreading and sliding velocity of droplets is also computed. Furthermore, the volume of the reconstructed 3D droplet is estimated versus time for validation.

2.4. Experimental procedure

All experiments presented in this section are carried out in *Kerberos*, an innovative device that allows the application of accurately controlled body forces to a droplet placed on top of a surface and provides full optical monitoring of the phenomena along with air temperature and moisture control ([29,30]). For the study of the droplet shape evolution, water droplets of 20 µL are evaluated as they slide over common microscope glass (hydrophilic surface) and Teflon (slightly hydrophobic surface). The droplet deposition over the substrate is made with a 500 µL syringe (1750 LTN SYR, Hamilton) attached to a repeating dispenser (PB600-1, Hamilton, step 1/50 of syringe volume). The image acquisition system comprises three wireless cameras (WCB-100 A, Brickcom, 10fps) distributed orthogonally around the droplet to record the phenomena from side, top and back views. Magnification lenses (x7, x14, x21) (Olloclip, 3 in 1 Lens) can be mounted on the cameras when higher image resolution is needed. The

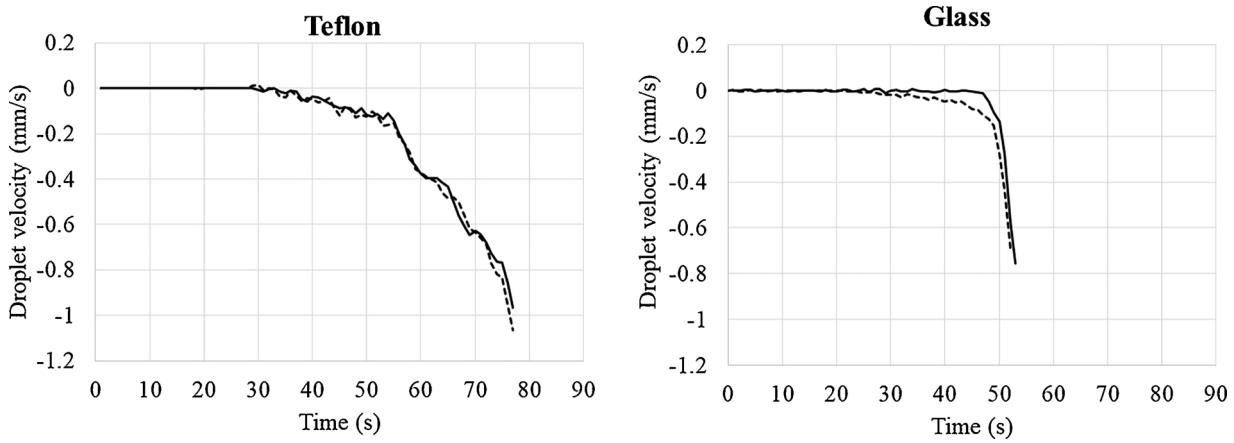

Fig. 16. Droplet velocity for a 20 μL droplet sliding over glass and Teflon. Front (dashed line) and rear (solid line) edge velocity. Rotational speed increases by 1 rpm/s.

three cameras are synchronized in time with each other. Supervisory Control and Data Acquisition software (SCADA) is implemented for the accurate synchronization of *Kerberos* operating parameters with the recorded videos.

A low concentration of "brilliant blue" (0.5 g/L, Hina Dye Chem Industries) is added to Millipore water (ultrapure water, Direct-Q, Merck Millipore) in order to enhance the contrast of top view images of droplets. By doing so, the accuracy of image analysis is increased leaving interfacial properties unaffected. Measurements of equilibrium and dynamic surface tension by the Wilhelmy plate (TE2, LAUDA) and maximum bubble pressure (BPA-1SX, Sinterface) methods show no difference between the dyed and non-dyed water. The same holds for the values of advancing and receding contact angles as measured by *Kerberos*. Although for the system under study the presence of a dye shows no effect on interfacial properties, this might not be the case for other systems in which adsorption of the dye particles onto the solid surface or modification of the liquid surface tension cannot be neglected. For these cases, an improved illumination system has been designed using a combination of different lighting angles from different locations around the droplet depending on the reflectivity of the substrate surface which can provide images with satisfactory contrast even without a dye. Nevertheless, the scope of this work is to demonstrate the capacity of the present software to reconstruct accurate 3D contours of droplets during spreading and sliding. The higher the contrast in top view images, e.g., as provided by the use of a dye, the higher the accuracy of the droplet contour reconstruction.

During the experiments, increasing centrifugal forces are applied to a droplet placed on top of a surface until the droplet sliding is noticed. The rotational speed is increased by 1 rpm/s until a target rotation speed is reached and then, the speed is kept constant until the end of the experiment. The target speed is the one for which the tangential acceleration applied to the system provokes droplet sliding. In these particular experiments, the target rotation speed depends on the solid under study (glass or Teflon).

3. Results and discussion

A set of experiments is carefully designed to evaluate the performance and explore the capabilities of the developed image-analysis software for the study of forced wetting. Several experiments are performed under different conditions in order to prove the adaptability of the new tool to different scenarios. For this purpose, experimental results using two solid substrates with different surface properties (i.e. glass: hydrophilic; and Teflon: slightly hydrophobic) are presented.

First, several 2D geometric features are obtained from side and top images. The droplet shape as expressed by the solid-liquid and liquid-vapor interfaces is evaluated through the examination of contact angles, droplet length, droplet height, contact points and highest point positions, droplet velocity and contour evolution.

Regarding the droplet movement, both spreading and sliding stages are easily identified in the water/glass system when either one edge (spreading) or both edges (sliding) of the droplet are set in motion. However, when forces are applied to a droplet placed over Teflon, the critical rotation speeds for spreading and sliding coincide and thus, all parts of the droplet detach and move simultaneously. The evolution of front (θ_f) and rear (θ_r) contact angles is shown in Fig. 10. Mild fluctuations in the estimated values represent experimental uncertainty plus computational errors. Front and rear parts of the droplet are defined with respect to the direction of the applied force. On the one hand, a 20 μL water droplet placed over a glass surface attains initially a contact angle of 40° at both edges. Advancing and receding contact angles are experimentally found to be around $\theta_A = 50°$ and $\theta_R = 10°$, respectively at the critical rotation speed $RS = 48$ rpm as shown in Fig. 10a. In this case, the contact angle hysteresis (CAH), defined as the difference between advancing and receding contact angles, is about 40°. On the other hand, a droplet of the same volume placed on Teflon attains initially a contact angle of 90° with the solid at both edges. Experiments reveal that advancing and receding contact angles are 100° and 80°, respectively, which implies 20° of hysteresis. In this case, the critical rotation speed for sliding is $RS = 35$ rpm as seen in Fig. 10b. In literature, Teflon contact angles can be found to vary from 110° to 115° [38,39]. This work, however, is not meant to deliver contact angle values for Teflon but only to allow comparison between the wetting performances of different materials and show the capacity of Kerberos and of the respective image analysis. In other words, the reported lower contact angles obtained for Teflon are circumstantial and do not represent exact measurements.

In the latter case (water/Teflon system) the initial contact angle value (90°) is in the middle between the advancing (100°) and receding (80°) contact angles and hence the movement of both edges occurs simultaneously. However, in the water/glass system, there is a difference of 10° between the initial and the advancing and 30° between the initial and the receding contact angle. Therefore, when increasing rotation, the droplet attains the advancing contact angle at its front before the receding angle is reached at its rear. As a results the droplet spreads from its front. The movement of the front part of the droplet with the rear part still pinned to the substrate provokes the elongation of the droplet and the increase of the liquid-solid contact area. The comparison of the elongation for both systems is shown in Fig. 11. The simultaneous movement of the two droplet edges while sliding over Teflon makes the elongation almost unnoticeable (Fig. 11(b)) unlike the droplet elongation over glass, where a 23% increase of droplet length is

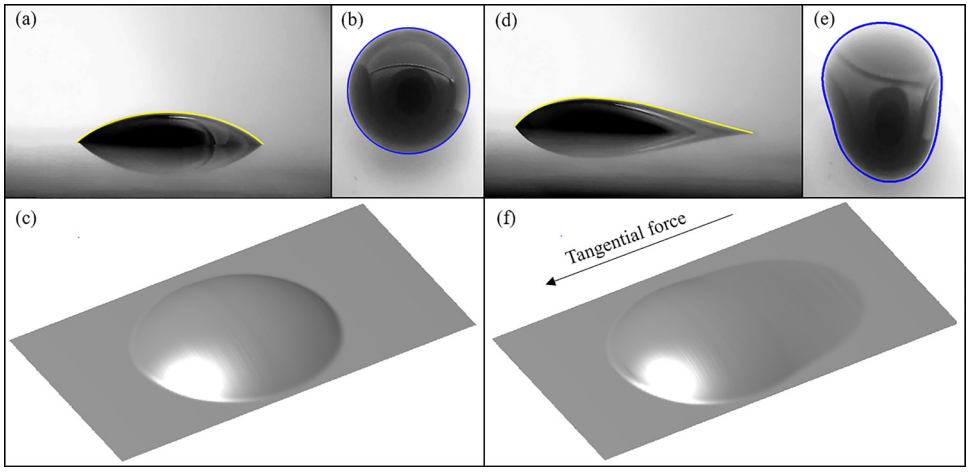

Fig. 17. Actual images from side and top views and the respective 3D reconstructions of a 20 μL droplet deposited on a glass substrate. (a) Initially axisymmetric droplet shape, (b) a sliding non-axisymmetric droplet shape.

measured (Fig. 11(a)). Comparing the initial droplet length ($t=0$) for both substrates confirms that the water droplet initially spreads to a larger extent in glass (5.75 mm initial length) than in Teflon (4.79 mm initial length).

Another parameter that can be studied to explore the droplet shape deformation is the droplet height. As already mentioned, when the droplet is placed over glass, it spreads just at the moment of contact with the solid. Due to this spontaneous spreading, the initial height of the droplet on glass is lower than on Teflon (opposite to the length). Inspecting now the height evolution versus time it is seen that the height of the droplet placed on glass decreases with the force as the length increases. However, for the droplet placed on Teflon, both length and height are essentially constant during all the sliding process (Fig. 11).

To explore in-depth the droplet position and its symmetry, the x-coordinate of the front and rear droplet edge is plotted versus time in Fig. 12 for the water/glass system. It is apparent that, at the beginning, the position of the edges does not change with time, thus the whole droplet is completely pinned in place. After the spreading critical rotation speed ($RS = 28$ rpm, $t = 28$ s) is reached the front edge moves in the direction of the force with the rear edge remaining pinned at its initial location. At $t = 48$ s, when the sliding critical rotation speed ($RS = 48$ rpm) is reached, the rear edge of the droplet moves, too, from its original position in the same direction. The dashed line in Fig. 12 represents the x-coordinate of the middle distance between the edges. Its comparison with the x-coordinate of the highest point gives a clue about droplet symmetry. At the beginning ($t = 0$ s) the x-coordinates of the droplet middle and highest points coincide indicating droplet symmetry. However, when the rotation speed is increased ($RS = 20$ rpm) the droplet deforms, and the highest point is not anymore in the middle but closer to the front edge.

The same information is plotted below (Fig. 13) for a droplet sliding on Teflon pointing out the simultaneous movement of both droplet edges ($t = 35$ s) and the persistent droplet symmetry during the whole process. Side view snapshots of the droplet are added to Figs. 12 and 13 to support the discussion about droplet symmetry.

For a more accurate study of droplet shape evolution, individual contours from side and top views are extracted and presented. In Fig. 14, the top (up) and side (bottom) contour evolution for a droplet sliding over glass reveals the significant deformation experienced by the droplet during spreading and sliding.

In Fig. 15, the droplet contour evolution for the water/Teflon system is observed. In this case, the droplet does not deform during the sliding process and keeps its initial circular shape when viewed from the top. The symmetry is also observed when the droplet side contours are analyzed.

When a water droplet spreads over glass, it elongates increasing the liquid-solid contact area. This elongation leads to an increasing friction between the liquid and the solid that retards the relative movement of the droplet over the glass. Due to this fact, the droplet sliding velocity is slower on glass than on Teflon, where the droplet keeps a smaller liquid-solid contact area during the whole process. Sliding velocity has been demonstrated to be a fundamental property in hydrophobic surface characterization [40]. The comparison of sliding velocities for a water droplet over glass and Teflon can be seen in Fig. 16. Spotting the velocity of the edges independently, one can notice, again, that the beginning of the movement for both edges is simultaneous for the droplet over Teflon whereas this is not so for the droplet over glass.

Apart from the extraction of 2D geometrical features, the software allows obtaining the 3D reconstruction of the droplet shape through combination of side and top images. In Fig. 17, snapshots of the actual side and top images and the respective 3D reconstruction are shown for an initially axisymmetric droplet (a) and for a non-axisymmetric droplet during sliding (b). Beside individual snapshots, the software permits video representation of the 3D reconstruction of droplet performance. An indicative 3D reconstruction of a droplet sliding over glass is presented as a supplementary material, S1.

Based on the 3D reconstruction, the contact angles along the perimeter can be computed to determine a more precise droplet shape. Fig. 18 displays the estimated contact angle distribution along the droplet perimeter for (a) axisymmetric droplet and (b) (sliding) non-axisymmetric droplet. In Fig. 18(a), the contact angle distribution around the droplet perimeter is approximately a straight line because the drop is axisymmetric and attains the same contact angle (40°) with the surface for all azimuthal coordinates. Nevertheless, in Fig. 18(b) the distribution of contact angles around the perimeter is not a straight line. The front part of the droplet attains the advancing contact angle ($\theta_A = 50°$), the rear attains the receding ($\theta_R = 10°$) and the angles for the intermediate positions vary from advancing to receding.

4. Conclusions

In the present work, a custom–made software for the analysis of droplet images lying on solid substrates is presented. This new tool is developed for the analysis of non-axisymmetric droplets created during forced wetting experiments in *Kerberos* ([29,30]). The wetting phenomenon is analyzed using images from two cameras placed orthogonally to each other that provide side and top view images of the droplet during the wetting process. Through the experimental comparison of droplet wetting over a hydrophilic and a slightly

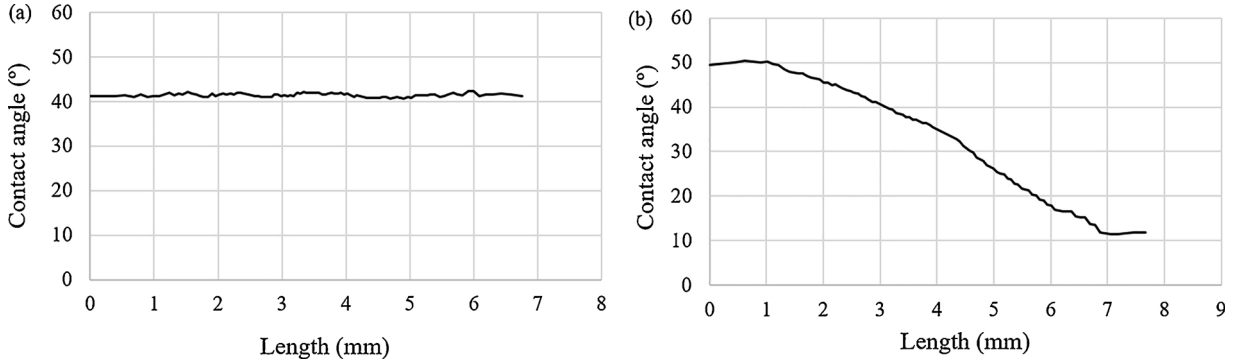

Fig. 18. Contact angle distribution around droplet perimeter for a 20 µL water droplet (a) axisymmetric shape (b) (sliding) non-axisymmetric shape.

hydrophobic substrate, evidence is provided on the capabilities of the new software to characterize droplet shape in terms of its solid-liquid and liquid-vapor interfaces under different wetting scenarios. In addition, tangential forces that need to be applied to induce droplet spreading and sliding on either substrates is examined. The study of the droplet shape and movement is carried out through i) extraction of 2D droplet geometrical features from side and top images providing information related to contact angles, droplet length, droplet height, edges position, droplet velocity, contour points; ii) droplet 3D shape reconstruction that avails the precise exploration of the droplet shape and the estimation of contact angles distribution along the droplet perimeter.

Acknowledgements

This work was supported by Marie-Curie ITS “Complex wetting Phenomena, CoWet” (FP7-PEOPLE-2013-ITN, grant number 607861).

Appendix A. Supplementary data

Supplementary material related to this article can be found, in the online version, at doi: https://doi.org/10.1016/j.colsurfa.2018.05.098.

References

[1] O. Arjmandi-Tash, N.M. Kovalchuk, A. Trybala, I.V. Kuchin, V. Starov, Kinetics of wetting and spreading of droplets over various substrates, Langmuir 33 (2017) 4367–4385, http://dx.doi.org/10.1021/acs.langmuir.6b04094.
[2] D. Biolè, M. Wang, V. Bertola, Assessment of direct image processing methods to measure the apparent contact angle of liquid drops, Exp. Therm. Fluid. Sci. 76 (2016) 296–305, http://dx.doi.org/10.1016/j.expthermflusci.2016.04.006.
[3] Y. Rotenberg, L. Boruvka, a.W. Neumann, The shape of non-axisymmetric bubbles on inclined planar surfaces, J. Colloid Interface Sci. 102 (1984) 424–434, http://dx.doi.org/10.1016/j.colsurfa.2013.10.040.
[4] T. Young, An essay on the cohesion of fluids, philos, Trans. R. Soc. Lond. 95 (1805) 65–87, http://dx.doi.org/10.1098/rstl.1805.0005.
[5] Y. Yuan, T.R. Lee, Contact angle and wetting properties, Surf. Sci. Tech. Springer-Verlag, Berlin Heidelberg, 2013, pp. 3–34, http://dx.doi.org/10.1007/978-3-642-34243-1.
[6] A. Marmur, Measures of wettability of solid surfaces, Eur. Phys. J. Spec. Top. 197 (2011) 193–198, http://dx.doi.org/10.1140/epjst/e2011-01457-4.
[7] D.Y. Kwok, a.W. Neumann, Contact Angle Measurement Contact Angle Interpretation, (1999), http://dx.doi.org/10.1016/S0001-8686(98)00087-6.
[8] V. Berejnov, R.E. Thorne, Effect of transient pinning on stability of drops sitting on an inclined plane, Phys. Rev. E - Stat. Nonlinear Soft Matter Phys. 75 (2007) 1–6, http://dx.doi.org/10.1103/PhysRevE.75.066308.
[9] A.B.D. Cassie, Contact angles, Discuss. Faraday Soc. 3 (1948) 11–16, http://dx.doi.org/10.1039/DF9480300011.
[10] O. Río, A. Neumann, Axisymmetric drop shape analysis: computational methods for the measurement of interfacial properties from the shape and dimensions of pendant and sessile drops, J. Colloid Interface Sci. 196 (1997) 136–147, http://dx.doi.org/10.1006/jcis.1997.5214.
[11] M. Hoorfar, A.W. Neumann, Recent progress in axisymmetric drop shape analysis (ADSA), Adv. Colloid Interface Sci. 121 (2006) 25–49, http://dx.doi.org/10.1016/j.cis.2006.06.001.
[12] M. Bortolotti, M. Brugnara, C. Della, S. Siboni, Numerical models for the evaluation of the contact angle from axisymmetric drop profiles : a statistical comparison, J. Colloid Interface Sci. 336 (2009) 285–297, http://dx.doi.org/10.1016/j.jcis.2009.03.055.
[13] L. Li, W. Kang, D. Ye, A contact angle measurement method for the droplets in EWOD-based chips, Proc. 2nd IEEE Int. Conf. Nano/Micro Eng. Mol. Syst. IEEE NEMS 2007 (2007) 1071–1075, http://dx.doi.org/10.1109/NEMS.2007.352203.
[14] G. Mchale, H.Y. Erbil, M.I. Newton, S. Natterer, Analysis of shape distortions in sessile drops, Langmuir 17 (2001) 6995–6998, http://dx.doi.org/10.1021/la010476b.
[15] S.F. Chini, A. Amirfazli, A method for measuring contact angle of asymmetric and symmetric drops, colloids surfaces a physicochem, Eng. Asp. 388 (2011) 29–37, http://dx.doi.org/10.1016/j.colsurfa.2011.08.001.
[16] M. Mirzaei, A new method for measuring the contact angles from digital images of liquid drops, Micron 102 (2017) 65–72, http://dx.doi.org/10.1016/j.micron.2017.09.001.
[17] E.B. Dussan V, The moving contact line: the slip boundary condition, J. Fluid Mech. 77 (1976) 665–684, http://dx.doi.org/10.1017/S0022112076002838.
[18] C.-J. Wu, V. Singh, Y.-J. Sheng, H.-K. Tsao, Forced spreading of aqueous solutions on zwitterionic sulfobetaine surfaces for rapid evaporation and solute separation, Langmuir (2017), http://dx.doi.org/10.1021/acs.langmuir.7b01384 acs.langmuir.7b01384.
[19] R.A. Brown, F.M. Orr, L.E. Scriven, Static drop on an inclined plate: analysis by the finite element method, J. Colloid Interface Sci. 73 (1980) 76–87, http://dx.doi.org/10.1016/0021-9797(80)90124-1.
[20] C.W. Extrand, A.N. Gent, Retention of liquid drops by solid surfaces, J. Colloid Interface Sci. 138 (1990) 431–442, http://dx.doi.org/10.1016/0021-9797(90)90225-D.
[21] C. Antonini, F.J. Carmona, E. Pierce, M. Marengo, A. Amirfazli, General methodology for evaluating the adhesion force of drops and bubbles on solid surfaces, Langmuir 25 (2009) 6143–6154, http://dx.doi.org/10.1021/la804099z.
[22] C.G.L. Furmidge, Studies at phase interfaces. I. The sliding of liquid drops on solid surfaces and a theory for spray retention, J. Colloid Sci. 17 (1962) 309–324, http://dx.doi.org/10.1016/0095-8522(62)90011-9.
[23] C.W. Extrand, Y. Kumagai, Liquid drops on an inclined plane: the relation between contact angles, drop shape, and retentive force, J. Colloid Interface Sci. 170 (1995) 515–521, http://dx.doi.org/10.1006/jcis.1995.1130.
[24] A.I. ElSherbini, A.M. Jacobi, Liquid drops on vertical and inclined surfaces: I. An experimental study of drop geometry, J. Colloid Interface Sci. 273 (2004) 556–565, http://dx.doi.org/10.1016/j.jcis.2003.12.067.
[25] L.N. Popova, Nonaxisymmetric equilibrium shapes of a drop on a plane, Fluid Dyn. 18 (1983) 634–637, http://dx.doi.org/10.1007/BF01090633.
[26] A. Carre, M.E.R. Shanahan, Drop motion on an inclined plane and evaluation of hydrophobic treatments to glass, J. Adhes. 49 (1995) 177–185, http://dx.doi.org/10.1080/00218469508014354.
[27] C.W. Extrand, S.In Moon, When sessile drops are no longer small: transitions from spherical to fully flattened, Langmuir 26 (2010) 11815–11822, http://dx.doi.org/10.1021/la1005133.
[28] P. Dimitrakopoulos, J.J.L. Higdon, On the gravitational displacement of three-dimensional fluid droplets from inclined solid surfaces, J. Fluid Mech. 395 (1999) 181–209, http://dx.doi.org/10.1017/S0022112099005844.
[29] S.P. Evgenidis, K. Kalić, M. Kostoglou, T.D. Karapantsios, Kerberos: a three camera headed centrifugal/tilting device for studying wetting/dewetting under the influence of controlled body forces, colloids surfaces a physicochem, Eng. Asp. (2016) 1–32, http://dx.doi.org/10.1016/j.colsurfa.2016.07.079.
[30] I. Ríos-lópez, S.P. Evgenidis, M. Kostoglou, T.D. Karapantsios, Effect of initial droplet shape on the tangential force required for spreading and sliding along a solid surface, Colloids Surf. A Physicochem. Eng. Asp. (2018).
[31] J. Canny, A computational approach to Edge detection, IEEE Trans. Pattern Anal. Mach. Intell. PAMI-8 (1986) 679–698, http://dx.doi.org/10.1109/TPAMI.1986.4767851.
[32] N. Otsu, A threshold selection method from gray-level histograms, IEEE Trans. Syst. Man. Cybern. SMC-9 (1979) 62–66 doi:0018-9472/79/0100-0062$00.75.
[33] S.J. Miller, The Method of Least Squares 1 (2004), pp. 1–3.
[34] R. Farebrother, Least absolute residual procedure, Int. Encycl. Stat. Sci. Springer, Berlin, Heidelberg, 2011, pp. 754–755, http://dx.doi.org/10.1007/978-3-642-04898-2.
[35] X. Chenyang, J.L. Prince, Gradient vector flow: a new external force for snakes, Proc. IEEE Comput. Soc. Conf. Comput. Vis. Pattern Recognit. 2 (1997) 66–71,

http://dx.doi.org/10.1109/CVPR.1997.609299.
[36] M. Kass, a. Witkin, D. Terzopoulos, Snakes: active contour models, Int. J. Comput. Vis. 1 (1988) 321–331, http://dx.doi.org/10.1007/BF00133570.
[37] M. Higashine, K. Katoh, T. Wakimoto, T. Azuma, Profiles of liquid droplets on solid plates in gravitational and centrifugal field, J. JSEM 8 (2008) 49–54, http://dx.doi.org/10.11395/jjsem.8.s49.
[38] Z.Q. Zhu, Y. Wang, Q.S. Liu, J.C. Xie, Influence of bond number on behaviors of liquid drops deposited onto solid substrates, Microgr. Sci. Technol. 24 (2012) 181–188, http://dx.doi.org/10.1007/s12217-011-9294-1.
[39] F.J.M. Ruiz-Cabello, M.A. Rodríguez-Valverde, M. Cabrerizo-Vílchez, A new method for evaluating the most stable contact angle using tilting plate experiments, Soft Matter. 7 (2011) 10457, http://dx.doi.org/10.1039/c1sm06196h.
[40] M. Sakai, A. Hashimoto, N. Yoshida, S. Suzuki, Y. Kameshima, Image analysis system for evaluating sliding behavior of a liquid droplet on a hydrophobic surface, Rev. Sci. Instrum. 045103 (2007) 1–5, http://dx.doi.org/10.1063/1.2716005.